Journal of Zhejiang University-SCIENCE A (Applied Physics & Engineering) in press
www.jzus.zju.edu.cn; www.springer.com/journal/11582
E-mail: jzus_a@zju.edu.cn

Research Article

https://doi.org/10.1631/jzus.A2300610

Dynamic performance of a high-speed train exiting a tunnel under crosswinds

Yanlin HU[1], Xin GE[2], Liang LING[1], Chao CHANG[1], Kaiyun WANG[1]✉

[1]*State Key Laboratory of Rail Transit Vehicle System, Southwest Jiaotong University, Chengdu 610031, China*
[2]*CRRC Qingdao Sifang Co., Ltd, Qingdao 266000, China*

Abstract: The dynamic performance of high-speed trains is significantly influenced by sudden changes in aerodynamic loads (ADLs) when exiting a tunnel in a windy environment. Focusing on a double-track tunnel under construction in a mountain railway, we established an aerodynamic model involving a train exiting the tunnel, and verified it in the FLUENT environment. Overset mesh technology was adopted to characterize the train's movement. The flow field involving the train, tunnel, and crosswinds was simulated using the Reynolds-averaged turbulence model. Then, we built a comprehensive train-track coupled dynamic model considering the influences of ADLs, to investigate the vehicles' dynamic responses. The aerodynamics and dynamic behaviors of the train when affected by crosswinds with different velocities and directions are analyzed and discussed. The results show that the near-wall side crosswind leads to sharper variations in ADLs than the far-wall side crosswind. The leading vehicle suffers from severer ADLs than other vehicles, which worsens the wheel-rail interaction and causes low-frequency vibration of the car body. When the crosswind velocity exceeds 20 m/s, significant wheel-rail impacts occur, and running safety of the train worsens rapidly.

Key words: High-speed train; Aerodynamic characteristics; Dynamic performance; Crosswind; Numerical simulation method

1 Introduction

With the continuous development of Chinese railway networks, railway construction is in progress in the central and western mountain regions. Due to the complex topography of these areas, a large number of tunnels are constructed to cross the mountains, and the maximum bridge-tunnel ratios of some mountain railway lines exceed 80%. The rolling mountains and complex topography greatly affect the speed and direction of natural winds (Bullard et al., 2000; Zhang et al., 2019). Moreover, the transition between tunnels and open-air sections applies additional aerodynamic loads (ADLs) to trains in crosswind environments (Li et al., 2017; Li et al., 2021). The sudden variation in ADLs has significant effects on the operational quality of vehicles (Sun et al., 2019). Therefore, it is of great significance to investigate the dynamic behavior of vehicles when a train exits a tunnel in a crosswind environment.

Field testing and simulation are the primary methods for analyzing the wind-related running safety of trains. Niu et al. (2017) field-tested the aerodynamic performance of different high-speed trains (HSTs) in crosswinds, with and without windbreaks. They used both field testing and dynamic simulation to study the dynamic responses of the HSTs to the scenario transformation that occurs under crosswinds. Liu et al. (2017a) measured the car-body lateral vibration responses when a HST passed through complex terrain sections, and observed a car-swaying phenomenon. Sun et al. (2018) measured the wheel-rail forces (WRFs) when a HST passed a windbreak breach in strong crosswinds. The derailment coefficient of the first wheelset on the windward side was found to reach the allowable value in the test. However, field tests have limitations. The safety of the HST must be ensured during testing, and environmental conditions are unpredictable, which makes it difficult to study the dynamic responses of a HST under extreme conditions by testing. As a result,

✉ Kaiyun WANG, kywang@swjtu.edu.cn
Yanlin HU, https://orcid.org/0000-0002-5558-9831
Kaiyun WANG, https://orcid.org/0000-0003-0958-4260

Received Dec. 1, 2023; Revision accepted Mar. 15, 2024;
Crosschecked

simulation is still the most commonly used method for analyzing the dynamic response of trains running in crosswind environments.

Determinations of ADLs and vehicle dynamic characteristics are the key elements for assessment of the operational quality of a HST during simulation. ADLs are typically obtained from wind-tunnel tests on reduced-scale models (Lu et al., 2020) or computational fluiddynamics (CFD) models (Yao et al., 2020). Vehicle dynamic characteristics are often simulated with vehicle dynamic models(Baker et al., 2011; Li et al., 2015). Using a full-scale field test and wind-tunnel test, along with CFD and vehicle system dynamics, Baker et al. (2009) designed a study framework for the effects of crosswinds on trains, and proposed risk-analysis methods for trains. Liu et al. (2020) investigated the influence of continuously varying wind speed on train overturning safety. The effects of interval time, wind-speed amplitude variation, wind-speed change rate, and peak wind-speed duration on train dynamic performance were analyzed. Liu et al. (2017b) studied the flow structure around a HST passing through a discontinuous windbreak transition region, and proposed a critical wind speed based on the EN14067-6. Deng et al. (2019) analyzed the ADLs on a HST travelling through tunnel and bridge infrastructures in crosswinds, and were able to determine the influence of wind speed and angle on time-resolved ADLs. Yang et al. (2020) analyzed the running safety of trains entering tunnels under crosswinds, using a single-vehicle dynamics model.

Because strong winds occur frequently in mountainous areas, the effect of crosswinds on the operational quality of HSTs in mountain railways is considered highly important. Sun at el. (2019) revealed that sudden loading of ADLs leads to more severe dynamic responses of vehicles compared to sudden unloading of ADLs. The HST will be exposed to higher safety risk when leaving a tunnel with crosswinds at the tunnel exit, which is worthy of special attention. Previous studies have devoted their attention to the operational quality of HSTs passing through different complex crosswind scenarios. However, studies on the aerodynamics and dynamic behaviors of a HST leaving a tunnel under crosswind conditions are still lacking, and the related investigations remain to be conducted.

This study focuses on a double-track tunnel under construction in a mountainous area of China. Using the CFD technology available in FLUENT software, we simulated the time-variant ADLs acting on vehicles when a train exits a tunnel and is subjected to crosswinds. A train-track coupled dynamic model was then formulated to calculate the dynamic responses of the vehicles influenced by crosswinds. The influence of the direction and velocity of crosswinds are analyzed and discussed. The goal of the study was to provide a reference for train operation in this complex environment.

2 Simulation models

To investigate the aerodynamics and dynamic performance of a train exiting a tunnel in a crosswind environment, we established a full-scale aerodynamic model of a HST passing through a tunnel in the FLUENT environment to obtain the ADLs applied to vehicles. We also built a detailed numerical dynamic model to calculate dynamic responses. The ADLs applied to vehicles were equivalently converted to the focused forces and moments applied to the car-body barycentre, and then imported into the dynamic model for dynamic analysis.

2.1 Aerodynamic model

2.1.1 Geometric model and meshing strategy

Fig. 1a shows the computational domain of a train traveling through a typical double-track tunnel with a total clear area of 81.4 m^2 in a Chinese mountain railway. The open-air regions at both ends of the tunnel are considered as two half-column spaces with a diameter of 121.5 m in the computational domain. The total length of the tunnel is 300 m, and the lengths of the open-air regions in front of the tunnel entrance and behind the tunnel exit are 300 m and 200 m, respectively. The geometric model of the HST consists of the leading, middle, and tail vehicles. The length, height, and width of the train model are 75 m, 4.05 m, and 3.36 m, respectively, and the barycenter of the car body is 1.67 m from the ground.

Non-slip walls in the model include the flat ground, both ends of the tunnel, and the train and tunnel surfaces. Standard wall functions are used at these walls. The atmospheric boundaries at the tunnel entrance and exit use the pressure-outlet and pres-

sure-far-field boundary conditions, respectively. Both ends of the computing domain in the longitudinal direction are set to the symmetry boundary conditions. The train running speed and direction are controlled by user-defined functions. The direction of crosswinds which are set at the pressure-far-field boundaries is perpendicular to the train running direction.

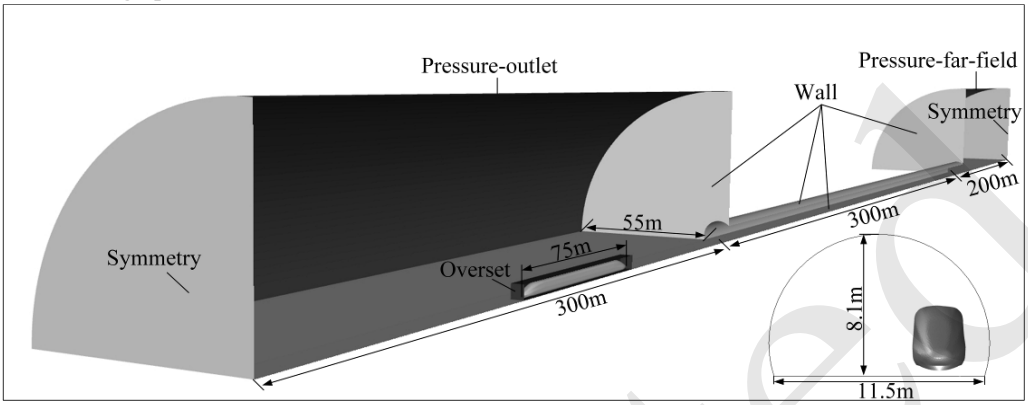

(a)

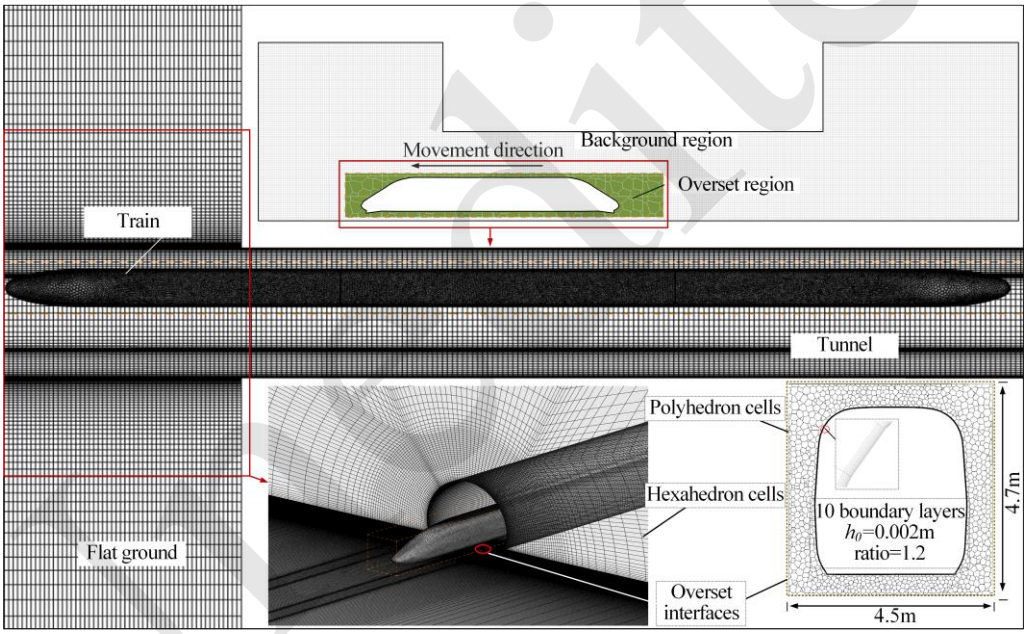

(b)

Fig. 1 Boundary conditions and mesh details of the computational domain: (a) computational domain of the aerodynamic model; (b) schematic diagram of mesh details

The motion of the train is characterized by employing the overset mesh technique. The computational domain consists of the foreground region (FR) and background region (BR), which are first meshed separately and then coupled to form the overset region, as shown in Fig 1b. The structural hexahedral cells are employed to discretize the BR, which includes the open air and tunnel space. The volume surrounding the train, i.e. the FR, is discretized by utilizing the polyhedral cells. The carriage surface is divided into a 10-layer boundary layer with a first-layer thickness of 2 mm and growth ratio of 1.2; correspondingly, the y^+ values are between 50 and 120. Meanwhile, the mesh size specified for the train surface ranges between 0.04 m and 0.09 m. To improve interpolation accuracy at the overset interfaces and better reflect the characteristics of the air flow near the train, the grid elements of the BR are refined in the train running direction to match the element size of the FR.

2.1.2 Computational method and simulation setups

In the simulation, the air is considered as the ideal compressible gas. As a HST passes through a tunnel or a crosswind environment, the air flow around it presents significant unsteady turbulence characteristics (Deng, et al., 2019). Reynolds-averaged Navier-Stokes (RANS) turbulence models have been employed to solve the flow field involving the train, tunnel, and crosswind. A previous study (Szudarek et al., 2022) revealed that there were no significant differences in the aerodynamic forces predicted by different RANS models when the yaw angle was below 45 degrees. As the resulting wind inflow angle was below 30 degrees in this study, a realizable k-ε turbulence model (Shih et al., 1995) was adopted to simulate the aerodynamic characteristics of the train exiting the tunnel in a crosswind environment.

Table 1 Details of computer specifications for simulation

Configuration	Specifications
System	Windows 10 (64 bit)
Software Version	Fluent 2021 R2
CPU	Intel(R) Xeon(R) Gold 6142 ×2
RAM	SAMSUNG DDR4 2666MHz 16GB ×8
Hard Drive	KSG60ZSE512G SATA 512GB & AVAGO MR9440-8i 4TB ×3

With a reasonable courant number and good convergence efficiency, the time-step size in the simulation was set as 5×10^{-3} s. The entire running time of the HST was about 9.2 s. Simulations were conducted on the workstation, and the computer specifications are listed in the Table 1. The average calculation time for each case (using 24 physical cores) was about 120.7 hours, including the time needed to save case and data files with an interval of 20 time-steps. The user-defined functions are employed to obtain the aerodynamic forces and moments. The calculation for each time step was regarded as completely convergent when the residuals of all variables descended to 10^{-4}, as all of the ADLs were in a steady state in the duration, and the residual error of energy remained below 10^{-7}.

2.1.3 Verification

We checked the mesh independence of this model by comparing target indicators for three meshing cases with different cell numbers. Side forces acting on the leading, middle, and tail car bodies were compared between case 1 (0.9×10^6 cells in FR and 7.0×10^6 cells in BR), case 2 (1.5×10^6 cells in FR and 10.2×10^6 cells in BR), and case 3 (2.3×10^6 cells in FR and 13.6×10^6 cells in BR). The speeds of the crosswind and train were 20.8 m/s and 200 km/h (55.6 m/s), respectively; and the resultant wind angle was 24 degrees. It can be seen in Table 2 that the target indicators for case 1 are obviously greater than those for case 2. However, the target indicators for cases 2 and 3 were highly similar. The side forces remained stable when the number of cells increased to 11.7×10^6. Therefore, we adopted the meshing scheme in case 2 to carry out the simulation.

Table 2 Effects of cell count on simulated side forces

Forces (kN)	Leading	Middle	Tail
Case 1	48.17	25.54	3.32
Case 2	46.11	23.71	2.01
Case 3	45.94	23.52	1.98

To verify the modeling methodology, we established a verification model using the same modeling method. Accordingly, the same mesh scheme was adopted to discretize the computational domain, as shown in Fig 2a.

We compared the time-variant pressure of the car-body surface obtained from the verification model with a full-scale field-test result reported by Liu et al. (2010). The measurement point was located outside the side window in the middle of the car body of the leading vehicle. The dimensions of the train geometric model were scaled to match those of the test train. Based on the test conditions, the length of the tunnel was set to 1320 m and the train speed was 200 km/h. The cross-section of the modelled tunnel was consistent with that of the test tunnel, and the velocity of the crosswind at the tunnel exit was regarded as 0 m/s.

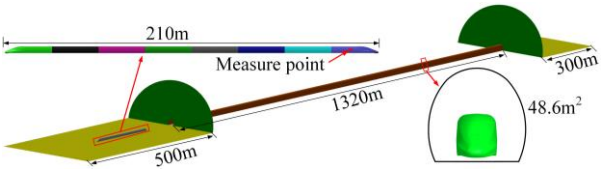

(a)

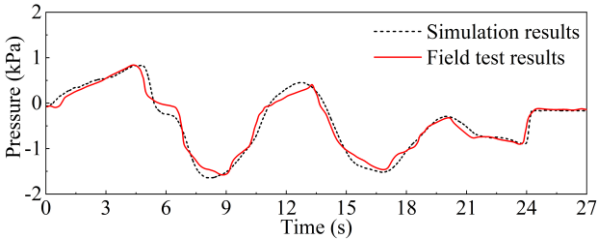

(b)

Fig. 2 Model validation: (a) schematic diagram of verification model; (b) comparison of simulation results and the test results reported by LIU et al. (2010).

Fig 2b presents a comparison between the transient pressure results obtained by simulation and by field testing. The simulated results generally accorded with the field-test results in terms of variation trends. As the train adopted for the model was not the same as that in the test, there were differences in geometry features between the two trains. Moreover, the simulation environment was ideal compared to the testing one; small differences between the simulation and test results could not be avoided. According to the results, the maximum positive and negative pressure error of the measurement point were 3.5 % and 2.7%, respectively, and the maximum peak-to-peak pressure error was 6.2%, which verified the reliability of the methodology. Therefore, the established aerodynamic model can accurately simulate the transient variation in the pressure around a train when it is passing through a tunnel.

2.1 Dynamic model

In this section, based on vehicle-track coupled dynamics theories (Iwnicki, 2020; Zhai, 2020), we established a detailed dynamic numerical model to simulate the transient and non-linear dynamic performance of a train in the situation, as shown in Fig 3.

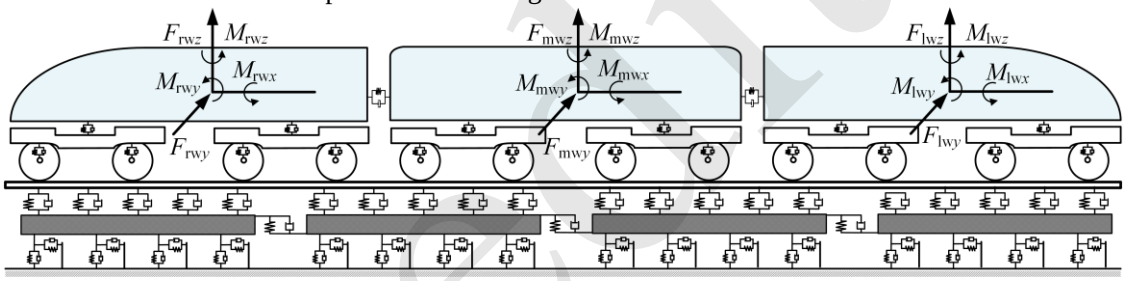

Fig. 3 The train-track coupled dynamic model. F and M with subscripts represent the aerodynamic forces and moments applied to vehicles, respectively.

The dynamic train model consists of three vehicles, which are connected to the adjacent vehicles by inter-vehicle components. Each vehicle is composed of seven rigid components, including the car body, two bogies, and four wheelsets, with 42 total degrees of freedom. We adopted spring-damper elements to model the primary and secondary suspension systems. More details of the model can be found in Refs (Ling et al., 2015; Ling et al., 2017b). The ADLs are considered as concentrated forces and moments, which are applied to the barycenter of car bodies. The governing equation of the coupled dynamic system can be constructed as follows.

$$\begin{bmatrix} \boldsymbol{M}_{\mathrm{V}} & 0 \\ 0 & \boldsymbol{M}_{\mathrm{T}} \end{bmatrix} \begin{Bmatrix} \boldsymbol{X}_{\mathrm{V}}'' \\ \boldsymbol{X}_{\mathrm{T}}'' \end{Bmatrix} + \begin{bmatrix} \boldsymbol{C}_{\mathrm{V}} & 0 \\ 0 & \boldsymbol{C}_{\mathrm{T}} \end{bmatrix} \begin{Bmatrix} \boldsymbol{X}_{\mathrm{V}}' \\ \boldsymbol{X}_{\mathrm{T}}' \end{Bmatrix} + \begin{bmatrix} \boldsymbol{K}_{\mathrm{V}} & 0 \\ 0 & \boldsymbol{K}_{\mathrm{T}} \end{bmatrix} \begin{Bmatrix} \boldsymbol{X}_{\mathrm{V}} \\ \boldsymbol{X}_{\mathrm{T}} \end{Bmatrix} = \begin{Bmatrix} \boldsymbol{F}_{\mathrm{V}} + \boldsymbol{F}_{\mathrm{WV}} \\ \boldsymbol{F}_{\mathrm{T}} \end{Bmatrix} \tag{1}$$

where $\boldsymbol{M}$, $\boldsymbol{C}$, and $\boldsymbol{K}$ with the subscripts V and T are the mass, damping, and stiffness matrices of the vehicle system and track system, respectively; $\boldsymbol{X}$ represents the generalized displacement vectors of components; $\boldsymbol{F}_{\mathrm{V}}$ and $\boldsymbol{F}_{\mathrm{T}}$ are vectors of the interactive forces and moments in the vehicle-track dynamics system; and $\boldsymbol{F}_{\mathrm{WV}}$ represents the wind-load vector. The key parameters of this dynamic model are listed in Table 3.

Table 3 Key parameters of the dynamic model

Parameters	Definition	Values
m_{c}	Car-body mass	3.66×10^{4} kg
m_{b}	Bogie mass	2.78×10^{3} kg
m_{w}	Wheelset mass	1.69×10^{3} kg
I_{cx}	Car-ody roll moment of inertia	1.18×10^{5} kg·m^{2}

I_{cy}	Car-body pitch moment of inertia	1.78×10^6 kg·m^2
I_{cz}	Car-body yaw moment of inertia	1.67×10^6 kg·m^2
k_{ssy}	Secondary suspension lateral stiffness	1.40×10^6 N/m
k_{ssz}	Secondary suspension vertical stiffness	1.25×10^6 N/m
k_{psy}	Primary suspension lateral stiffness	6.47×10^6 N/m
k_{psz}	Primary suspension vertical stiffness	1.28×10^6 N/m
k_{ksx}	Anti-hunting damper stiffness	8.82×10^6 N/m
H_{cr}	Height of the car-body center from the rail profile	1.67 m
H_{br}	Height of the bogie center from the rail profile	0.61 m
H_{wr}	Height of the wheelset from the rail profile	0.46 m

The models of inter-vehicle components, including the dampers and couplers, were established according to the Ref (Ling et al., 2017a), and were simulated as the nonlinear three-dimensional spring-damper elements.

We used the modified spatial model (Zhai et al., 2009) to solve the geometric relationship of the wheel and rail, which enabled us to calculate the dynamic contact point between the wheel and rail and handle the separation of wheels and rails. The FASTSIM algorithm (Kalker, 2007) was adopted to calculate the creep forces, which is considered a reasonable method for derailment simulations (Vollebregt et al., 2012). Considering a unilateral-restraint nonlinear Hertzian contact spring, the normal contact forces between wheel and rail could be written as follows:

$$F_{nc}(t)=\begin{cases}\left[\dfrac{1}{G_{nc}}Z_{nc}(t)\right]^{3/2}, & \text{if } Z_{nc}(t)>0,\\ 0, & \text{if } Z_{nc}(t)\le 0.\end{cases} \tag{2}$$

where F_{nc} represents the wheel-rail normal force (N) at time t; G_{nc} is the Hertzian contact constant (m/N$^{2/3}$); and Z_{nc} represents the normal compression amount at the wheel-rail contact point (m).

3 Aerodynamic loads on HST

In this section, we discuss the ADLs on car bodies in the time domain when the train exits the tunnel and is subjected to crosswinds with different velocities. The difference between the variations of ADLs caused by the near-wall side (NS) and far-wall side (FS) crosswinds is investigated. Concretely, a NS crosswind means that the crosswind is from the direction of the near-wall side (referring to the position of the train in a double-track tunnel), while a FS crosswind is from the opposite direction.

3.1 Influence of wind velocities

Based on minimum wind velocities of the wind scale of levels 7-10, we set the crosswind velocities to 13.9 m/s (W_1), 17.2 m/s (W_2), 20.8 m/s (W_3), and 24.5 m/s (W_4). The resulting wind angles were 14, 17, 21, and 24 degrees, respectively. The crosswind at the NS was set with a wind angle of 90 degrees, and the train speed was 200 km/h (55.6 m/s). Fig 4 shows the ADLs acting on the vehicles at different velocities. The leading vehicle began to enter the open air at t = 5.86 s, and the time difference for ADLs applied to adjacent vehicles was about 0.45 s, which is related to train speed and vehicle length.

It can be seen that ADLs fluctuate slightly as the train approaches the tunnel exit. In addition, the asymmetrical flow field around the running train in the double-track tunnel leads to the initial F_y, M_x and M_z applied to vehicles. However, these variations of ADLs in the tunnel are much smaller than those caused by crosswinds in the open air. Meanwhile, there was a phase delay in the flow when a vehicle was exposed to a sudden crosswind (Volpe et al., 2014), resulting in a time delay for stabilization of the ADLs. For example, the leading vehicle left the tunnel completely at t = 6.31 s, but the F_y applied to the vehicle stabilized at t = 6.68 s, as shown in Figure 4a$_1$. After the vehicle had been out of the tunnel for around 45.6 m, all the ADLs stabilized.

Some differences can be observed by comparing the ADLs exerted on the three vehicles. Firstly, the most significant variations in the F_y, M_x, and M_z occurred for the leading vehicle, followed by the middle vehicle, while the tail vehicle suffered the lowest ADLs. Moreover, the lift forces applied to the leading and tail vehicles were similar when the wind velocity was greater than W_2, and both of them were larger than those applied to the middle vehicle. The difference between the changes in pitching moments of the

three vehicles is significant, but the variation amplitude of all the pitching moments is within 180 kN·m. In addition, the steady-state ADLs on the leading vehicle are the largest among all vehicles.

For the leading vehicle, ADLs are mainly caused by the blocking effect of the car body to the cross-wind, which appears to be significantly correlated with wind velocities. However, variation in wind velocities changes the resulting wind angle, which significantly affects the generation of separation flow and vortex at the leeward side of the train. The complex flow-field structures are mainly located at the middle and tail parts of the train, resulting in wind-speed-related nonlinear variations in ADLs applied to rearward vehicles (Zhou et al., 2023).

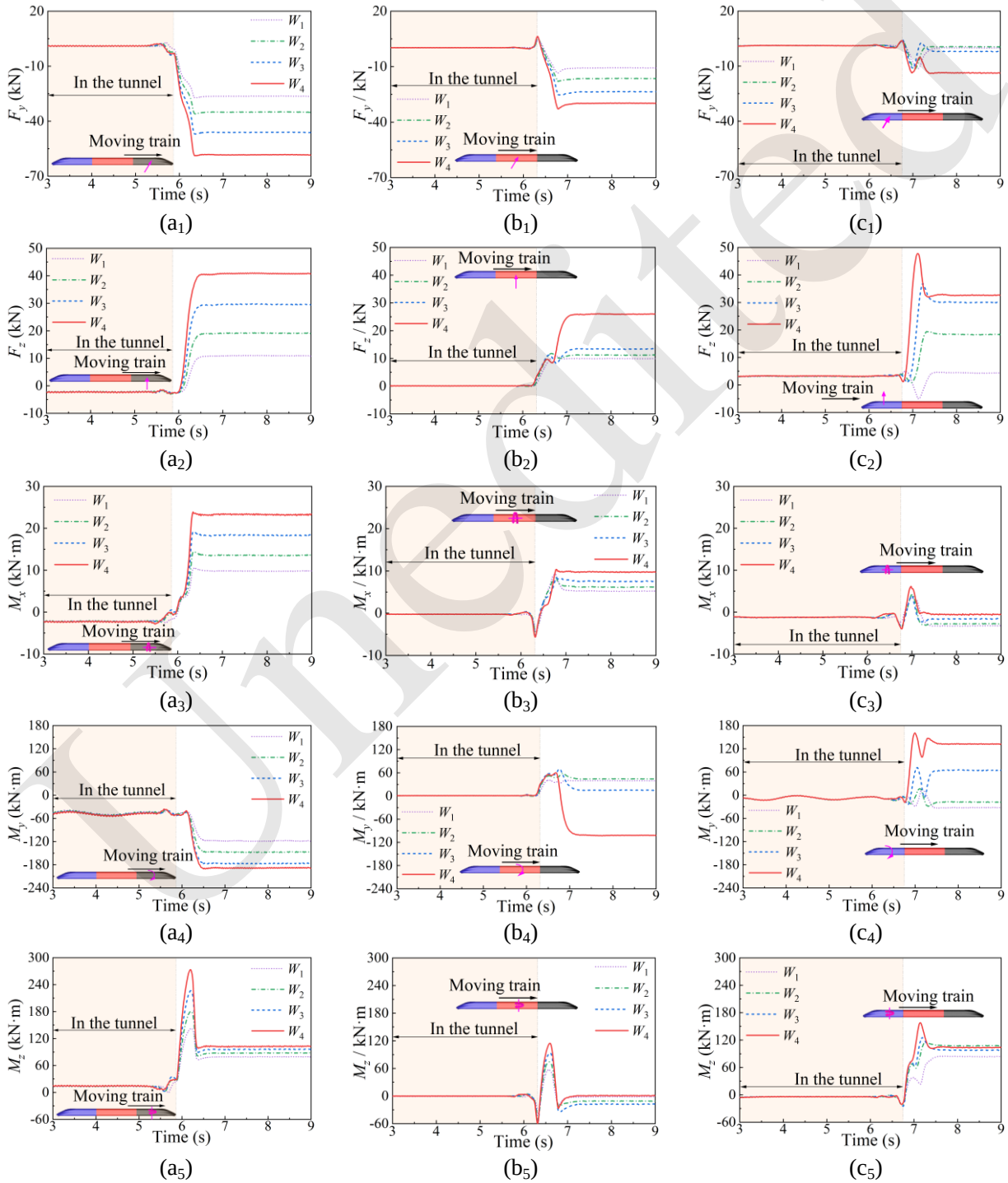

Fig. 4 ADLs applied to vehicles subjected to crosswinds of different velocities. a, b and c represent the leading, middle and tail vehicles, respectively; subscripts 1-5 represent the side and lift forces, rolling, pitching and yawing moments, respectively. The orange area in each panel represents the length of time vehicles run in the tunnel. The side and lift forces, and rolling, pitching, and yawing moments, are represented by F_y, F_z, M_x, M_y, and M_z, respectively

For the middle vehicle (Fig $4b_1$ − $4b_5$), load fluctuation increased with the increase of wind velocity, except for M_y. The M_y in steady-state was smallest when the wind velocity was W_3. As the wind speed reached W_4, the changes in F_z and M_y were especially sharp, and the direction of M_y changed as well. For the tail vehicle (Fig $4c_1$ − $4c_5$), both F_y and M_x fluctuated within a small range at wind velocities of W_1−W_4. F_z and M_y exhibited sensitivity to changes in wind velocity, and the instantaneous F_z on the tail vehicle was even larger than that on the leading vehicle when the wind velocity was greater than W_3. The differences between the steady-state yawing moments applied to the leading and tail vehicles are small. However, the peak values of the yawing moments applied to the leading vehicle are much greater than those for the tail vehicle.

3.2 Influence of crosswind direction

Fig 5 presents the ADLs on the leading vehicle when subjected to crosswinds from different directions. For an intuitive display of the value differences in ADLs caused by NS and FS crosswinds, the directions of F_y, M_x, and M_z caused by the FS crosswind are reversed in Fig 5a, 5c, and 5e.

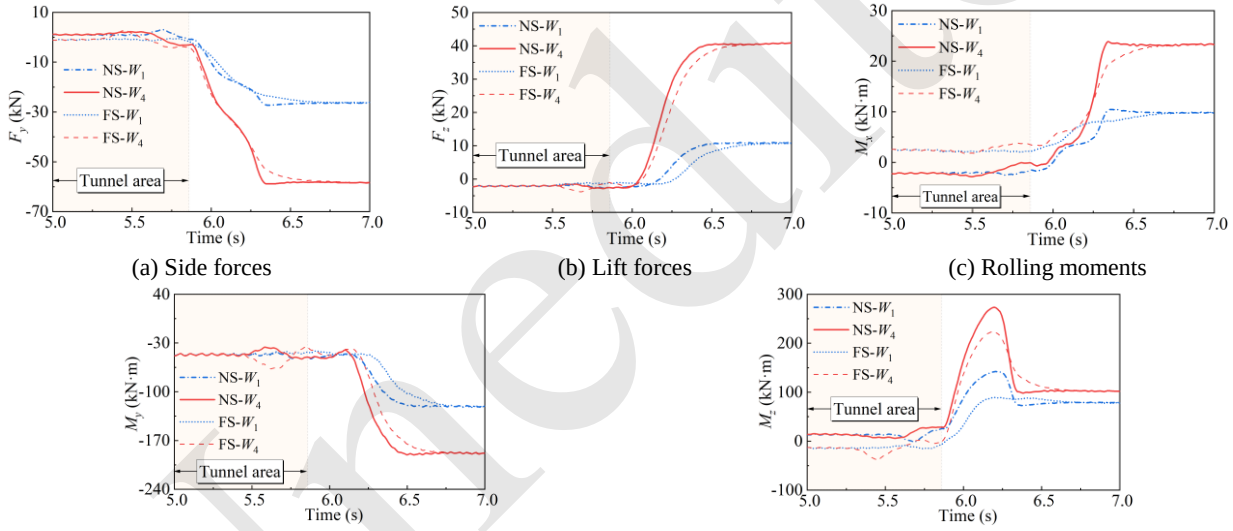

(a) Side forces (b) Lift forces (c) Rolling moments

(d) Pitching moments (e) Yawing moments

Fig. 5 The ADLs on the leading vehicle subjected to crosswinds with different directions

It can be seen that the NS crosswind causes greater variations in F_y and M_x compared to the FS crosswind. For example, when the wind speed is W_4, the F_y resulting from the NS crosswind reaches a peak of 58.7 kN at t = 6.34 s, while the F_y caused by the FS crosswind is 52.8 kN at the same time. In contrast, when the train approaches the tunnel exit, the fluctuations in F_y and M_x caused by the FS crosswind are slightly larger than those caused by the NS crosswind. However, these fluctuations within the tunnel are much smaller than those caused by crosswinds in open air.

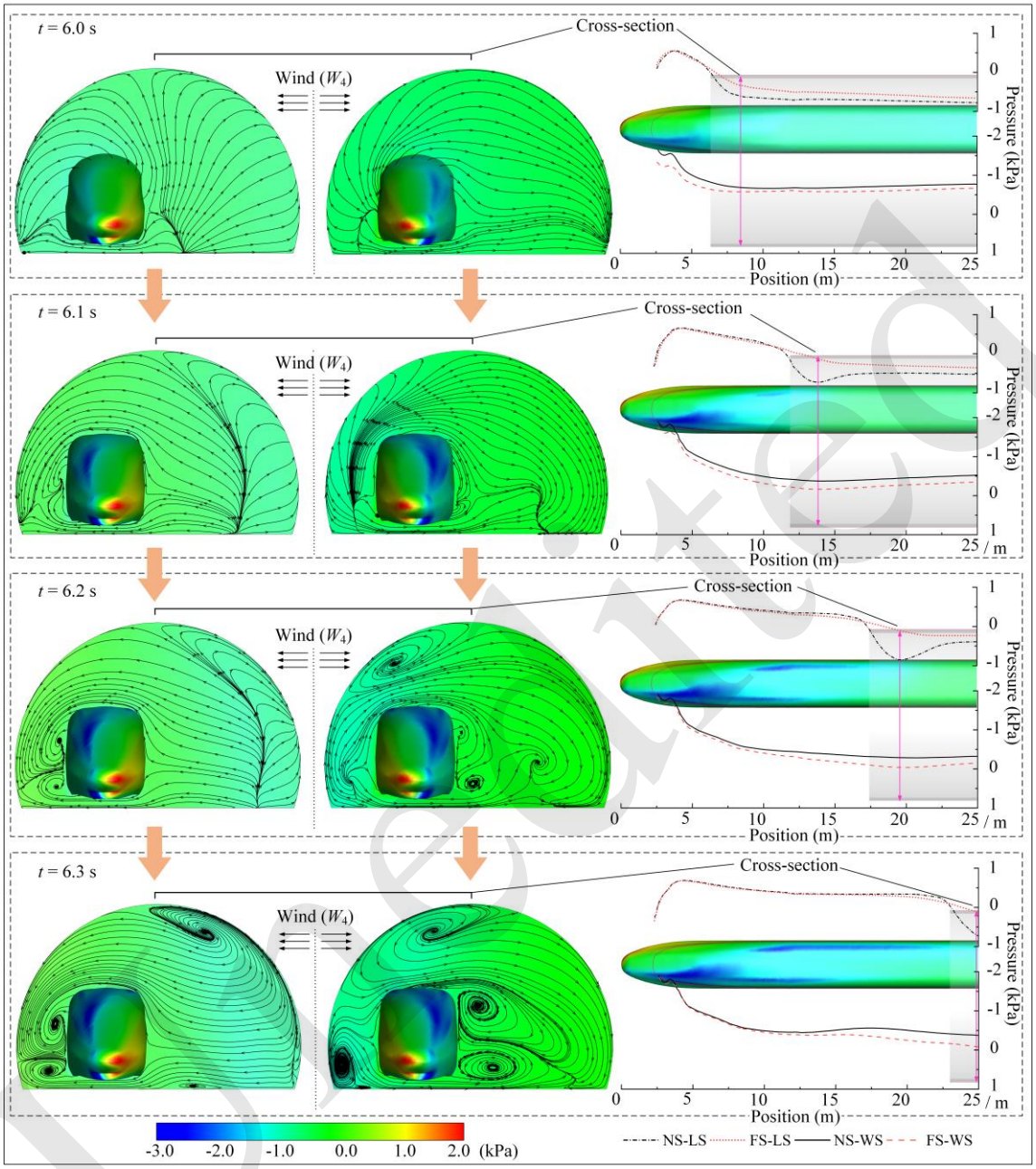

Fig. 6 Schematic diagram of pressure distribution around the leading vehicle at t = 6.0 – 6.3s

Fig 6 shows the aerodynamic characteristics of the leading vehicle when exiting the tunnel at t = 6.0 – 6.3 s with a wind speed of W_4. Specifically, the figure shows the static pressure on the car body at the intersection of the car-body surface and the plane, which is 2.5 m above the ground. The car-body surface with pressure distribution marked on it (in the NS crosswind condition) is used to reference the relative position of the tunnel exit and the leading vehicle. During the process, one part of the leading vehicle is affected by the crosswind while the other part remains inside the tunnel. In open air, the pressure distribution caused by the NS and FS crosswinds at the windward side (WS) of the vehicle is similar. However, compared to the FS crosswind condition, the value of negative pressure at the leeward side (LS) of the vehicle is significantly larger when the crosswind is set at the NS. The differences between the negative pressures decrease as the train moves forward. As a result, the side force and yawing moment caused by

the NS crosswind change more dramatically compared to those caused by the FS crosswind.

Inside the tunnel, there is little difference between WS and LS pressures on the vehicle, regardless of crosswind direction. However, there is a negative pressure zone adjacent to the in-tunnel part of the vehicle, which leads to a force applied on the corresponding part of the car body towards the WS (e.g., at t = 6.2 s) under NS crosswind conditions. By contrast, the negative pressure zone is located near the tunnel wall on the WS under FS crosswind conditions, which has little effect on the loads applied to the vehicle. This situation further aggravates the yawing moment applied to the leading vehicle when affected by the NS crosswind.

4 HST dynamic performance analysis

Based on the dynamic model formulated in Section 2 and the calculated ADLs from Section 3, we further analyzed the dynamic performance. An unloaded train consisting of three vehicles was adopted in the numerical simulation. The Chinese high-speed ballastless track spectrum is adopted for track excitations.

Fig 7 presents the vibration characteristics of car bodies when the HST comes out of a tunnel under the effects of a crosswind with a speed of W_3. As shown in Fig 7a and 7b, the sudden change in ADLs at the tunnel exit greatly affects the vibration acceleration of the car bodies. The car-body acceleration of the leading vehicle also fluctuates more severely than that of other vehicles, with maximum lateral and vertical accelerations of 2.2 m/s^2 and 0.7 m/s^2, respectively. Compared to the tail vehicle, the car body of the middle vehicle has a smaller amplitude of vertical acceleration and a greater amplitude of lateral acceleration.

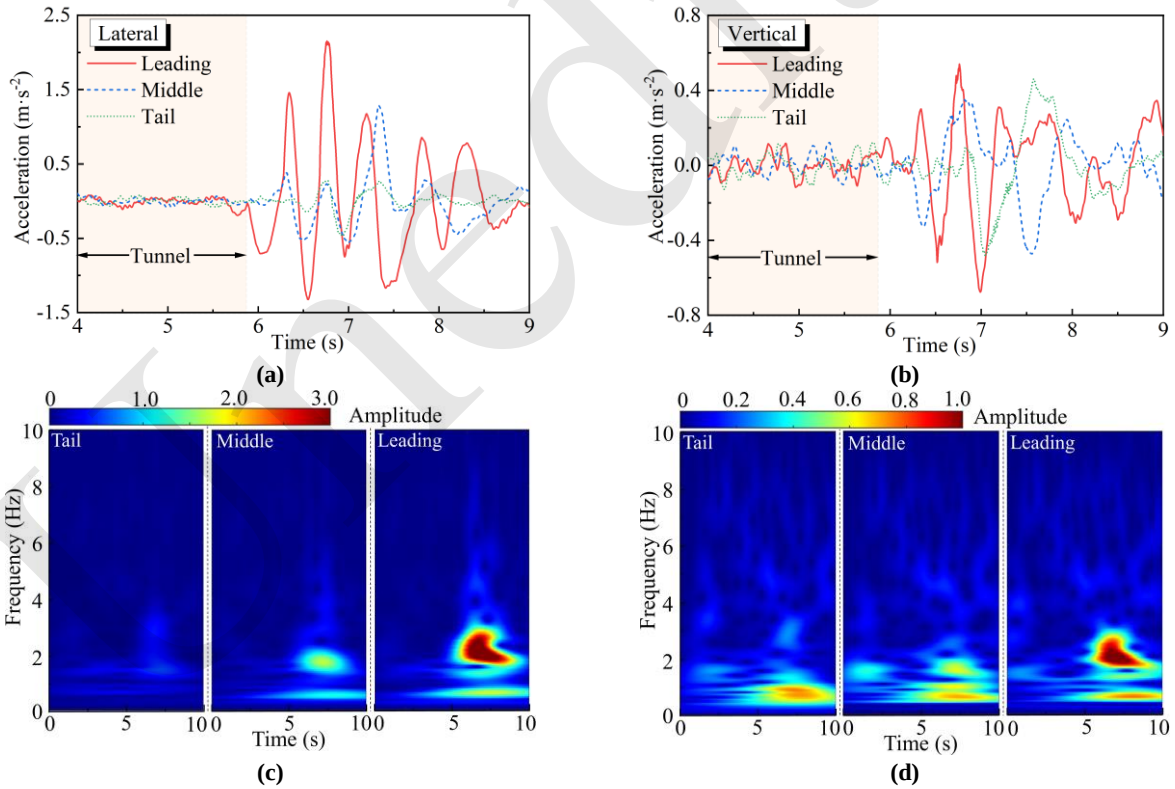

Fig. 7 Vibration acceleration of car bodies: (a) lateral acceleration; (b) vertical acceleration; (c) time-frequency diagram of lateral acceleration; (d) time-frequency diagram of vertical acceleration

The simulation results for car-body vibration acceleration are plotted on the time-frequency diagram in Fig 7c and 7d. It can be seen that the sudden changes in ADLs lead to low-frequency vibration of car bodies, and the vibration energy of the middle and tail vehicles is significantly lower than that of the leading vehicle. For the leading vehicle, the energy-concentrating area is obviously darker than for

other vehicles, and the vibration frequency falls within the range of 0.5 – 1.0 Hz and 1.6 – 3.0 Hz. As the vehicle enters open air and ADLs stabilize, the vibration energy within the frequency range of 1.6 – 3.0 Hz decreases rapidly, while that in the range of 0.5 – 1.0 Hz decays relatively slowly.

Focusing on the leading vehicle, Fig 8 further shows the kinematic relations between the car body, the frame of the first bogie, and the first wheelset. As the leading vehicle exits the tunnel and is subjected to the crosswind, the yawing moment increases rapidly and reaches its peak at around t = 6.2 s. Correspondingly, the car body yaws towards the LS, thereby restricting the bogie frame and wheelset from moving in the same direction. The lateral displacement of the wheel reaches its first peak at around t = 6.4 s. Then, the yawing moment weakens suddenly, while other loads remain at a minor level. The yaw angle of the car body decreases to near 0 rad under suspension forces. Subsequently, the sideward ADLs increase quickly and cause the car body to move to the LS. The bogie frame and wheelset are also compelled to move to the LS, resulting in a second peak of lateral wheelset displacement which is larger than the first peak. Meanwhile, it can also be observed that the lateral movement of the wheelset is limited by the LS rail at around t = 7 s. This indicates that the effect of the transient variation in the yawing moment on wheel-rail interaction is limited when the train exits the tunnel subject to a crosswind with a speed of W_3.

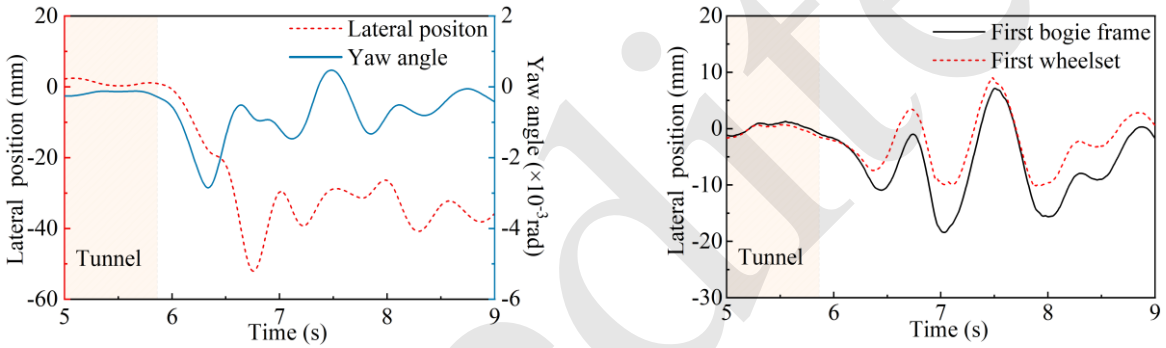

Fig. 8 Dynamic motion of the: (a) car body; (b) bogie frame and wheelset.

The WRFs of the vehicles are presented in Fig 9. The crosswind is from the NS at a speed of W_3, and the focus is on the first wheelset. Compared to the other vehicles, the wheel-rail interaction of the leading vehicle is especially intense. The sudden change in ADLs leads to more severe impacts between the wheels and rails, as significant wheel-rail impacts mainly occur upon the vehicle exiting the tunnel. When the vehicle is exposed to the stabilized ADLs, these severe wheel-rail interactions tend to be mitigated.

On the LS, WRFs of the leading and middle vehicles periodically fluctuate as the vehicle moves in open air. The initial peak in WRFs is clearly greater than subsequent peaks. The fluctuation of WRFs also decreases as the vehicle moves forward. We found that some wheel-rail impacts occur at t = 6.9 s – 7.9 s. However, we did not observe any similar impacts after t = 8.0 s. These results indicate that the sudden change in ADLs can aggravate the wheel-rail interaction, but when ADLs stabilize, the wheel-rail impacts caused by the transient ADLs gradually disappear, and the wheel-rail interaction is also mitigated.

On the WS, an obvious decrease in wheel loads is observed for the leading and middle vehicles. In particular, the vertical WRFs of the leading vehicle decrease to 0 kN at around t = 7.0 s, indicating separation of the wheels and rail. The sudden change in ADLs has a significant impact on the running safety of the leading vehicle. Compared to the middle vehicle, the variations of pitching moments applied to the tail vehicle are similar, while the lift force on the tail vehicle changes even more intensely. However, the fluctuations in WRFs for the tail vehicle are much smaller than those for the middle vehicle. This suggests that the intense wheel-rail interactions are mainly caused by the lateral ADLs.

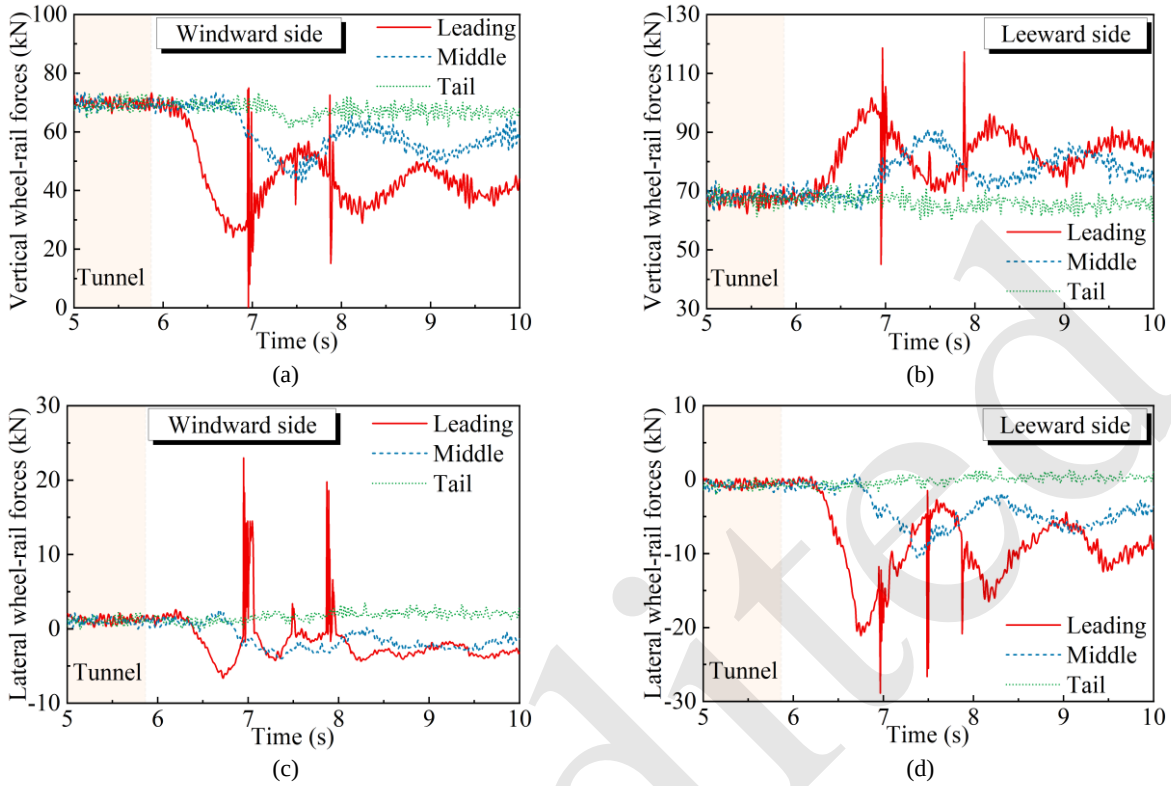

Fig. 9 WRFs of the first wheelset

Figure 10a and 10b present the maximum values of the vertical and lateral WRFs of the first wheelset. These values increase with increasing wind velocity, and the NS crosswind leads to a greater wheel-rail impact compared to the FS crosswind. The maximum WRF values caused by the FS and NS crosswinds are not obvious when the crosswind speed is below W_2. However, differences rapidly increase as wind speed continues to rise. At a wind speed of W_3, the differences in the lateral and vertical WRFs reach 9.2 kN and 18.5 kN, respectively.

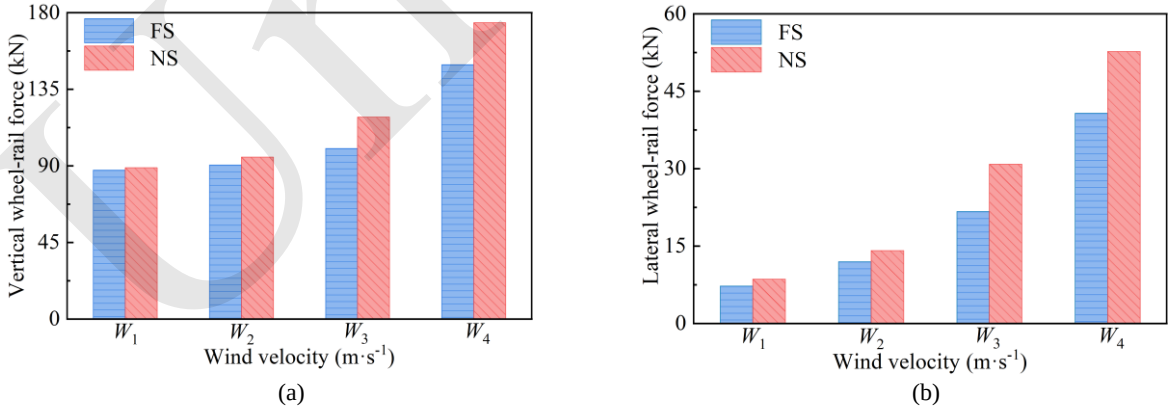

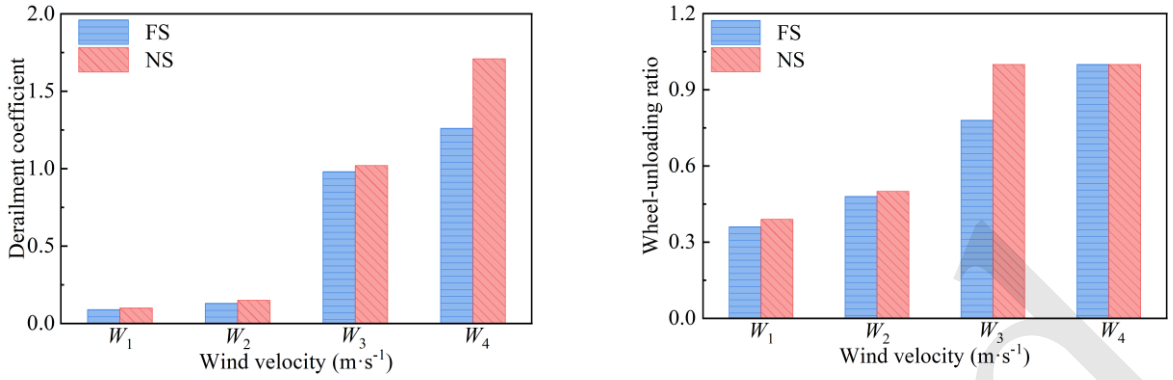

Fig. 10 Maximum statistics of WRFs and safety indices of the first wheelset

Figure 10c and 10d show the maximum values for the derailment coefficients and wheel unloading ratios, respectively. The derailment coefficients of the first wheelset are far below than the safety limit when the wind speed is below W_2. As the wind speed reaches W_3, the maximal derailment coefficient approaches 1, indicating a high running risk. Meanwhile, the maximal wheel-unloading ratio also attains 1 under the effects of the NS crosswind at a speed of W_3, and wheel-rail separation occurs under these conditions; while the corresponding indicator with a crosswind from the FS is 0.78, which is still under the safety limit (Cnra-Prc, 2019)(GB/T 5599-2019).

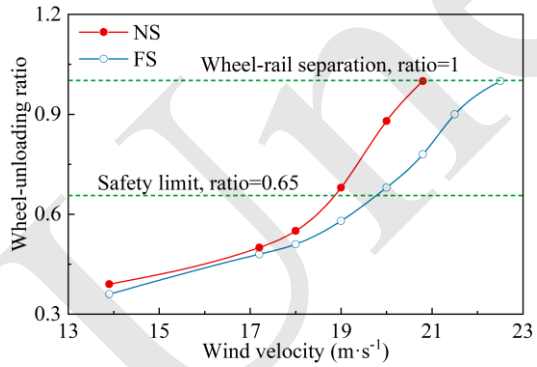

Fig. 11 Maximum wheel-unloading ratio of the first wheelset under different crosswind conditions

Fig 11 shows the maximum wheel-unloading ratio of the first wheelset under different wind conditions. The results show that the wheel-unloading ratio exceeds the safety limit when the velocities of NS and FS crosswinds increase to 19 m/s and 20 m/s, respectively, indicating a high safety risk for the leading vehicle. As the crosswind velocity exceeds 20 m/s, wheel-rail separation occurs when the train exits the double-track tunnel and is subjected to a NS crosswind. However, the velocity of a FS crosswind resulting in wheel-rail separation is about 22 m/s. Thus, a NS crosswind causes more severe wheel-rail interaction problems compared to a FS crosswind.

5 Conclusions

Here, we carried out an investigation on the aerodynamics and dynamic behaviors of a train exiting a double-track tunnel under crosswind conditions. We established an aerodynamic model in FLUENT software to obtain the time-variant aerodynamic loads applied to vehicles, and built a train-track coupled dynamic model to analyze the dynamic responses of vehicles. Accordingly, the following main conclusions can be drawn:

1. The sudden change in the infrastructure scenario leads to severe fluctuations in ADLs when a HST exits the tunnel into open air with strong crosswinds. The leading vehicle is exposed to the severest impact of ADLs, and the fluctuation in ADLs increases with increasing wind velocity.

2. The near-wall side crosswind leads to more severe changes in transient ADLs than the far-wall side crosswind. A NS crosswind leads to higher negative pressure on the leeward side of the leading vehicle in open air than does a FS crosswind. Meanwhile, the crosswind from the NS induces a negative pressure region adjacent to the vehicle at the WS, resulting in a force that is directed towards the WS applied to the corresponding part of the car body.

3. Sudden variations in ADLs aggravate the wheel-rail forces at the tunnel exit, and the fluctuation

amplitude of these forces decreases as ADLs stabilize. A NS crosswind leads to greater wheel-rail impacts compared to a FS crosswind. As the speed of the NS wind exceeds 19 m/s, the transient impact of ADLs at the tunnel exit can critically worsen the wheel-rail interaction, to the detriment of the running safety of the train, while the FS crosswind speed to ensure the running safety is below 20 m/s. In addition, sudden changes in ADLs result in a low-frequency vibration of car bodies within the frequency range of 0.5 – 3.0 Hz.

Further work could investigate effective methods to improve the operational quality of a train suffering from the transient impact of ADLs. The effects of the wind-break wall and tunnel hood on reducing the influence of crosswinds at tunnel exits should be a focus. Additionally, bogies and the surrounding topography should be thoroughly taken into account when analyzing the aerodynamic model.

Acknowledgments

This work is supported by the National Natural Science Foundation of China (grant No.52388102) and the New Cornerstone Science Foundation through the XPLORER PRIZE.

Author contributions

Yanlin HU designed the research and wrote the first draft of the manuscript. Chao CHANG processed the corresponding data. Xin GE helped to organize the manuscript. Liang LING and Kaiyun WANG revised and edited the final version.

Conflict of interest

Yanlin HU, Xin GE, Liang LING, Chao CHANG, and Kaiyun WANG declare that they have no conflict of interest.

Data availability statement

The data used to support the findings of this study are available from the corresponding author upon request.

References

Baker C, Cheli F, Orellano A, et al., 2009. Cross-wind effects on road and rail vehicles. *Vehicle System Dynamics*, 47(8):983-1022. https://doi.org/10.1080/00423110903078794

Baker C, Hemida H, Iwnicki S, et al., 2011. Integration of crosswind forces into train dynamic modelling. *Proceedings of the Institution of Mechanical Engineers, Part F: Journal of Rail and Rapid Transit*, 225(2):154-164. https://doi.org/10.1177/2041301710392476

Bullard J, Wiggs G, Nash D, 2000. Experimental study of wind directional variability in the vicinity of a model valley. *Geomorphology*, 35(1-2):127-143. https://doi.org/10.1016/s0169-555x(00)00033-7

CNRA-PRC (People's Republic of China National Railway Admin-istration), 2019. Specification for dynamic performance assessment and testing verification of rolling stock, GB/T 5599-2019, People's Republic of China National Railway Administration, Beijing, China.

Deng E, Yang W, Deng L, et al., 2019. Time-resolved aerodynamic loads on high-speed trains during running on a tunnel–bridge–tunnel infrastructure under crosswind. *Engineering Applications of Computational Fluid Mechanics*, 14(1):202-221. https://doi.org/10.1080/19942060.2019.1705396

Iwnicki S, Spiryagin M, Cole C, et al., 2020. Handbook of railway vehicle dynamics. translators, CRC Press, Boca Raton, USA, p.242–278.

Kalker J, 2007. A fast algorithm for the simplified theory of rolling contact. *Vehicle System Dynamics*, 11(1):1-13. https://doi.org/10.1080/00423118208968684

Li S, Zheng Z, Yu J, et al., 2015. Dynamic simulation and safety evaluation of high-speed trains meeting in open air. *Acta Mechanica Sinica*, 32(2):206-214. https://doi.org/10.1007/s10409-015-0471-0

Li W, Liu T, Martinez-Vazquez P, et al., 2021. Aerodynamic effects of a high-speed train travelling through adjoining & separated tunnels. *Tunnelling and Underground Space Technology*, 113:103973. https://doi.org/10.1016/j.tust.2021.103973

Li Y, Hu P, Xu X, et al., 2017. Wind characteristics at bridge site in a deep-cutting gorge by wind tunnel test. *Journal of Wind Engineering and Industrial Aerodynamics*, 160:30-46. https://doi.org/10.1016/j.jweia.2016.11.002

Ling L, Xiao X, Jin X, 2015. Development of a simulation model for dynamic derailment analysis of high-speed trains. *Acta Mechanica Sinica*, 30(6):860-875. https://doi.org/10.1007/s10409-014-0111-0

Ling L, Dhanasekar M, Thambiratnam D, 2017a. Frontal collision of trains onto obliquely stuck road trucks at level crossings: Derailment mechanisms and simulation. *International Journal of Impact Engineering*, 100:154-165. https://doi.org/10.1016/j.ijimpeng.2016.11.002

Ling L, Zhang Q, Xiao X, et al., 2017b. Integration of car-body flexibility into train–track coupling system dynamics analysis. *Vehicle System Dynamics*, 56(4):485-505. https://doi.org/10.1080/00423114.2017.1391397

Liu D, Lu Z, Zhong M, et al., 2017a. Measurements of car-body lateral vibration induced by high-speed trains negotiating complex terrain sections under strong wind conditions. *Vehicle System Dynamics*, 56(2):173-189. https://doi.org/10.1080/00423114.2017.1357828

Liu D, Li T, Tao Y, et al., 2020. The effect of continuously varying wind speed on high-speed train overturning safety. *Proceedings of the Institution of Mechanical Engineers, Part F: Journal of Rail and Rapid Transit*,

235(6):774-786. https://doi.org/10.1177/0954409720965813

Liu T, Tian H, Liang X, 2010. Aerodynamic effects caused by trains entering tunnels. *Journal of Transportation Engineering*, 136(9):846-853. https://doi.org/10.1061/(asce)te.1943-5436.0000146

Liu T, Chen Z, Zhou X, et al., 2017b. A CFD analysis of the aerodynamics of a high-speed train passing through a windbreak transition under crosswind. *Engineering Applications of Computational Fluid Mechanics*, 12(1):137-151. https://doi.org/10.1080/19942060.2017.1360211

Lu Y, Wang T, Yang M, et al., 2020. The influence of reduced cross-section on pressure transients from high-speed trains intersecting in a tunnel. *Journal of Wind Engineering and Industrial Aerodynamics*, 201:104161. https://doi.org/10.1016/j.jweia.2020.104161

Niu J, Zhou D, Liang X, 2017. Numerical investigation of the aerodynamic characteristics of high-speed trains of different lengths under crosswind with or without windbreaks. *Engineering Applications of Computational Fluid Mechanics*, 12(1):195-215. https://doi.org/10.1080/19942060.2017.1390786

Shih T, Liou W, Shabbir A, et al., 1995. A new *k-ε* eddy viscosity model for high reynolds number turbulent flows. *Computers & Fluids*, 24(3):227-238. https://doi.org/10.1016/0045-7930(94)00032-t

Sun Z, Dai H, Gao H, et al., 2018. Dynamic performance of high-speed train passing windbreak breach under unsteady crosswind. *Vehicle System Dynamics*, 57(3):408-424. https://doi.org/10.1080/00423114.2018.1469777

Sun Z, Dai H, Hemida H, et al., 2019. Safety of high-speed train passing by windbreak breach with different sizes. *Vehicle System Dynamics*, 58(12):1935-1952. https://doi.org/10.1080/00423114.2019.1657909

Szudarek M, Piechna A, Prusiński P, et al., 2022. CFD study of high-speed train in crosswinds for large yaw angles with rans-based turbulence models including geko tuning approach. *Energies*, 15(18):6549. https://doi.org/10.3390/en15186549

Vollebregt E, Iwnicki S, Xie G, et al., 2012. Assessing the accuracy of different simplified frictional rolling contact algorithms. *Vehicle System Dynamics*, 50(1):1-17. https://doi.org/10.1080/00423114.2011.552618

Volpe R, Ferrand V, Da Silva A, et al., 2014. Forces and flow structures evolution on a car body in a sudden crosswind. *Journal of Wind Engineering and Industrial Aerodynamics*, 128:114-125. https://doi.org/10.1016/j.jweia.2014.03.006

Yang W, Deng E, Zhu Z, et al., 2020. Sudden variation effect of aerodynamic loads and safety analysis of running trains when entering tunnel under crosswind. *Applied Sciences*, 10(4):1445. https://doi.org/10.3390/app10041445

Yao Z, Zhang N, Chen X, et al., 2020. The effect of moving train on the aerodynamic performances of train-bridge system with a crosswind. *Engineering Applications of Computational Fluid Mechanics*, 14(1):222-235. https://doi.org/10.1080/19942060.2019.1704886

Zhai W, Wang K, Cai C, 2009. Fundamentals of vehicle–track coupled dynamics. *Vehicle System Dynamics*, 47(11):1349-1376. https://doi.org/10.1080/00423110802621561

Zhai W, 2020. Vehicle–track coupled dynamics: Theory and applications. Springer Singapore, Singapore, p.17-149.

Zhang J, Zhang M, Li Y, et al., 2019. Comparison of wind characteristics at different heights of deep-cut canyon based on field measurement. *Advances in Structural Engineering*, 23(2):219-233. https://doi.org/10.1177/1369433219868074

Zhou D, Xia C, Wu L, et al., 2023. Effect of the wind speed on aerodynamic behaviours during the acceleration of a high-speed train under crosswinds. *Journal of Wind Engineering and Industrial Aerodynamics*, 232:105287. https://doi.org/10.1016/j.jweia.2022.105287

中文概要

题　目：高速列车横风下驶出隧道动力学性能研究

作　者：胡彦霖[1]，阎鑫[2]，凌亮[1]，昌超[1]，王开云[1]

机　构：[1]西南交通大学，轨道交通运载系统全国重点实验室，中国成都，610031；[2]中车青岛四方机车车辆股份有限公司，中国青岛，266000

目　的：高速列车在强风环境驶出隧道会受到突变气动载荷影响。本文旨在探讨风速和风向对车辆气动特性和动力学性能的影响，研究横风和隧道综合影响下的车辆运行安全性，以期为工程实践提供参考。

创新点：1. 探究了风向对车辆驶出双线隧道时的气动特性和动力学响应的影响规律；2. 通过列车–轨道耦合动力学模型确定了影响行车安全的风速限值。

方　法：1. 采用经验证的建模方法建立高速列车驶出隧道的气动特性分析模型，计算列车驶出隧道过程中作用于车身的时变气动载荷；2. 根据车辆实际动力学参数建立列车–轨道耦合动力学模型分析时变载荷影响下车辆的动力学响应特征；3. 统计与分析不同风速和风向条件下车辆的轮轨安全性指标，确定影响行车安全的风速阈值。

结　论：1. 作用于头车的气动载荷冲击最大，且与风速呈较明显正相关关系；2.双线隧道近墙侧来风导致更大幅度的瞬态气动载荷变化，对行车安全影响更大；3.突变气动载荷引起车身 0.5–3.0 Hz 的低频晃动，风速超过 20 m/s 将使头车运行安全性迅速恶化。

关键词：高速列车；空气动力学特性；动力学性能；横风；
数值仿真